

# A novel method to identify hydraulically-forced crevassing at ice shelves and glaciers

T.S. Hudson<sup>1\*</sup>, A.M. Brisbourne<sup>2</sup>, R.S. White<sup>3</sup>, J.M. Kendall<sup>1</sup>, R. Arthern<sup>2</sup>, A.M. Smith<sup>2</sup>

<sup>1</sup> *Department of Earth Sciences, University of Oxford, Oxford, UK*

<sup>2</sup> *British Antarctic Survey, Cambridge, UK*

<sup>3</sup> *Bullard Laboratories, University of Cambridge, Cambridge, UK*

## Abstract

Hydraulically-forced crevassing is thought to reduce the stability of ice shelves and ice sheets, affecting structural integrity and providing pathways for surface meltwater to the bed. However, direct observations of the physical processes associated with hydraulically-forced crevassing remain elusive. Here we report a new method that uses icequakes, that is seismic energy released due to a sudden change in strain within the ice, to directly observe crevassing and determine the role of hydrofracture. This method comprises of deriving crevasse icequake depths from seismic observations and comparing these depths to a theoretically derived maximum-dry-crevasse-depth. We also present icequake source mechanism results that provide insight into the fracture process. Source mechanisms are found to be predominantly opening cracks, with volumes of opening of the order of tens to hundreds of cubic metres. Our method and findings provide a framework for studying a critical process, which key for the stability of ice shelves and ice sheets, and hence rates of future sea-level rise.

## Introduction

Hydraulically-forced surface crevassing, also referred to as hydrofracture, has the potential to significantly influence the stability of glaciers, ice sheets and ice shelves. On glaciers and ice sheets, hydraulically-forced crevassing provides a potential pathway for surface meltwater to reach and lubricate the bed <sup>1-3</sup>, enhancing basal sliding of ice into the ocean <sup>4</sup>, accelerating sea-level rise. Hydraulically-forced surface crevassing on ice shelves can result in catastrophic failure, with melt ponds and other sources of surface meltwater promoting fracture that can lead to the collapse of the ice shelf <sup>5-8</sup>. Following ice shelf collapse, land-based glaciers can accelerate into the ocean, since the buttressing provided by the ice shelf no longer exists, again contributing to sea-level rise. Understanding the fundamental mechanism of hydraulically-forced surface crevassing is therefore a particularly pressing topic within glaciology.

Here, we present icequake observations from Skeidararjökull, an outlet glacier of the Vatnajökull Ice Cap, Iceland. This glacier is a suitable environment for studying potential hydraulically-forced crevassing due to the high levels of surface melt present. Icequakes are caused by a sudden stress release, with their source mechanisms providing insight into the fundamental mode of failure, whether that be via shear or tensile fracture. Previous studies have used icequakes to infer hydraulically-forced crevassing using auxiliary information, such as glacier speed up<sup>9</sup>, or the presence of meltwater<sup>10,11</sup>. Others have used seismicity to show that crevassing exhibits tensile faulting<sup>12-15</sup>. We first present a novel method for attributing an icequake to either dry or hydraulically-forced crevassing, providing evidence that the icequakes we observe are

likely induced by hydrofracture. We then demonstrate that icequake source analysis can confirm the crevassing stress release mechanism. Our results therefore provide insight into this previously elusive process.

## **Evidence for dry fracture vs. hydrofracture from crevasse depth**

As a crevasse propagates, the ice fractures, releasing seismic energy as icequakes. Crevasses ordinarily only propagate to a certain depth within the ice column, where the tensile stress field causing crevasse opening is compensated by the ice overburden pressure acting to close the crevasse. We refer to this depth limit as the maximum-dry-crevasse-depth,  $d^*$ . However, if the crevasse contains sufficient water, the additional pressure of this water column can overcome the ice overburden pressure and induce hydrofracture, allowing the crevasse to propagate to greater depths<sup>2,16</sup>. Therefore, if the observed depth of a crevasse icequake is greater than  $d^*$ , then one can infer that the icequake is induced by hydrofracture. This is the fundamental premise of this study.

However, obtaining sufficiently accurate icequake hypocentral depths for comparison to  $d^*$  is non-trivial. Seismometer networks are inherently poor at constraining the depth of an earthquake using traditional body wave methods if the source-receiver epicentral distance is much greater than the source depth. This is generally the case in our study. Since the depth of an icequake is critical evidence for or against hydrofracture, a more accurate method is required for constraining hypocentral depth. We therefore use surface wave information in the form of P-wave to Rayleigh wave amplitude ratios to constrain hypocentral depth<sup>17–20</sup>. Figure 1a shows finite-difference full-waveform

modelling results <sup>21</sup> and observations of P to Rayleigh amplitude ratios, plotted against epicentral distance for a range of crevasse depths. The observed amplitude ratios are compared to the model results to calculate the crevassing depths. We independently verify these crevasse depths using P-S delay-times from receivers close to the source epicentre where possible, giving us confidence that the amplitude ratios provide a sufficiently accurate estimation of icequake depth.

The observed crevassing depths constrained by the observations in Figure 1 can then be compared to the maximum-dry-crevasse-depths, shown in Figure 2b, which are derived from the surface velocity field shown in Figure 2a. Figure 2c shows the epicentral locations of the near surface seismicity, with the grey scatter points showing the automatically detected icequakes<sup>22</sup> and the coloured scatter points showing a subset of manually relocated events. The majority of this subset of icequakes are located below  $d^*$  (solid red line, Figure 2d), from which we infer that they may be induced by hydrofracture. However, we cannot definitively state that the events are associated with hydrofracture since the icequakes lie within the uncertainty bounds of  $d^*$  (dashed red lines, Figure 2d).

One potential limitation of using the source depth to discriminate between hydrofracture and dry fracture is that we do not account for dynamic rupture, whereby during the rupture itself, a crack may be able to propagate deeper than the prevailing stress field otherwise allows, due to instability initiated at the fracture tip<sup>23</sup>. For the purposes of this study we treat each icequake as an instantaneous point source, therefore neglecting dynamic rupture. Although this assumption is does not fully



describe the physics of the source, we deem it appropriate within the limits of this study because of the distinct, high-frequency and short-duration phase arrivals observed.

In the absence of more information and given that the events are predominantly deeper than  $d^*$ , we suggest that the majority of these events are likely caused by hydraulically-forced crevassing. In any case, the methodologies developed here, which constrain icequake depth from amplitude ratios and use this source depth to discriminate hydrofracture, are important developments for studying the physics of hydrofracture-induced crevassing.

### **Crevassing source mechanisms**

Moment tensor inversions constrain whether icequake source mechanisms include explosive, implosive, crack, or shear components. The icequake magnitude can also be used to calculate either the volume of opening, or fault area and displacement, depending upon the icequake source mechanism.

Figure 2c shows the P-wave-constrained moment tensor inversion results for the subset of icequakes for which sufficiently accurate depths have been obtained. The inversion results for two of these icequakes are presented in more detail in Figure 3. For both icequakes, the waveform polarities are all correctly inverted for. At a number of stations, later complexity in the observed waveforms is reproduced in the modelled waveforms. Lune plots<sup>24</sup> in Figure 3b and Figure 3d indicate that the most likely source mechanisms for the two icequakes are a closing and an opening crack, respectively, with

a negligible shear component in both cases. Such crack mechanisms are the mode of failure one might expect from either dry or hydraulically-forced crevassing. However, after considering the Probability Density Function (PDF) of the inversion solutions for the closing crack icequake in Figure 3b, an opening crack mechanism cannot be eliminated. This ambiguity is due to station geometry on the focal sphere, which could give a moment tensor solution similar to that in Figure 3c. In any case, an opening or closing crack of a specific orientation is required to represent the observations adequately, as inferred from previous seismic observations<sup>12-15</sup>.

All the opening and closing crack orientations of the icequakes in Figure 2c agree with the principal stress directions calculated from the observed surface velocities, as shown by the orange vectors in Figure 2c. This confirms interpretations in previous studies<sup>25,26</sup>. The apparent closing crack observation for the icequake at 64.327° N, 17.21° W may be supported by the presence of tensile stresses in both principal stress directions. In such a stress regime, a closing crack may well be a valid source mechanism, effectively exhibiting two-dimensional necking in the surface-parallel plane.

We calculate the moment magnitude of the crevassing icequakes using a spectral method<sup>27</sup>. Moment magnitudes range from -0.4 to -0.9. If we approximate all the failure as tensile, then for a tensile strength of ice of 1.5 MPa<sup>28</sup>, the volume associated with crack opening or closing is of the order of 30 m<sup>3</sup> to 150 m<sup>3</sup>.

We propose several possible mechanisms for generating seismicity below the maximum-dry-crevasse-depth. These interpretations are summarised in Figure 4. The

mechanisms are: (1) new opening cracks formed when the combined deviatoric near-surface stress field and hydrostatic pressure are sufficient to overcome the ice overburden pressure and tensile strength of the ice; (2) cracks opening on pre-existing crevasse fractures that have closed are reopened by a sufficient column of water in the crevasse; (3) pre-existing cracks that have been opened by water reclosing as the water is evacuated from the fracture, due to a preferential pressure gradient below the fracture.

For mechanisms 2 and 3, the crevasse must have propagated to that depth via mechanism 1, therefore suggesting that at least some of the icequakes we observe are likely to be new ice fracture. We observe principal tensile stress amplitudes of greater than 200 kPa (see Figure S2), more than sufficient to overcome an ice tensile strength of  $\sim 100$  kPa<sup>29</sup>. Mechanism 2 is similar to mechanism 1, except requiring a lower hydrostatic pressure to induce crack opening, and is possible if crevasses have formed upstream and subsequently been closed by a region of principal compressive stress perpendicular to the crevasse. Such refracturing is proposed in scenarios where there are insufficient volumes of surface meltwater to immediately establish a permanent bed connection<sup>30</sup>. Mechanism 3 is presented more tentatively, partly because there is potential ambiguity of the solution due to relatively poor spatial sampling of the source mechanism inversion (see Figure 3a), but also because these crevasses would have to close over sufficiently short time scales to generate the  $\sim 100$  Hz source frequencies that we observe in the P-wave spectra. While it is conceivable that the ice can suddenly fail or reopen a crack over such a short duration, a possible source of driving stresses or pressures required to close cracks this quickly is less conceivable. One could imagine a crack at greater depth reopening and causing a sufficient pressure gradient to evacuate

water from a cavity above, but it is difficult to conceive of the driving stress or pressure that opens this lower crack being sufficiently localised so as not to inhibit the closing-crack. The only viable mechanism we suggest is that water travels through an opening, pre-existing crack sufficiently quickly that the crack then empties and closes almost immediately. If the closing crack has a higher signal to noise ratio seismic signature than the opening crack then it may dominate the seismic signal in our data. In summary, we therefore confidently present mechanisms 1 and 2, but suggest that mechanism 3 is unlikely.

One question that arises is why we do not observe seismicity via mechanism 1 or 2 occurring all the way to the glacier bed, as is proposed in various studies<sup>1,2,10,30,31</sup>. The most likely reason is that as such fractures penetrate deeper into the glacier, the energy will be more attenuated and fall below background noise levels. Any intermediate depth icequakes would likely not be detected and located reliably using our dataset. Therefore, we cannot say whether or not the hydrofracture propagates to the bed in our case.

These results emphasise the potential information that icequakes hold for elucidating the physics of hydrofracture of glaciers. Here, we have only used P waves to constrain the mechanisms, but if one had a more comprehensive dataset with a greater number of receivers and higher SNR, then it may be possible to constrain the source mechanism better. Furthermore, if one were to invert for a dynamic rupture model of finite length, rather than the instantaneous point source that we assume here, then one might gain additional insight into the physics governing hydrofracture in ice. Another approach to learn more about the hydrofracture process could be to compare observations such as

ours to theoretical models of crevasse vibrational modes to infer crevasse geometry<sup>32</sup>,  
or even models of supraglacial lake drainage<sup>33</sup>.

## **Implications for ice sheet and ice shelf stability**

Our findings provide a method for observing hydrofracture at icesheets such as the  
Greenland Ice Sheet, where although it has been shown that meltwater can drain from  
the surface to the bed<sup>3</sup>, the mechanism and pathway has not been imaged previously.  
Calving at the ocean termini of outlet glaciers of the Greenland Ice Sheet could also be  
enhanced by hydrofracture. Increased calving could be facilitated by precipitation  
increasing the hydrostatic pressure of water-filled crevasses<sup>34</sup>, or by damage to the  
upstream ice<sup>35</sup>, with the depth of this damage through the ice column dependent upon  
the depth of the crevasses, which we infer here to be controlled by the glacier stress  
state and hydrofracture. Our method could provide observations of the depth of such  
damage. The above mechanisms are also hypothesised to be important factors that  
could accelerate the collapse of the West Antarctic Ice Sheet and cause significant  
retreat of the East Antarctic Ice Sheet<sup>36</sup>.

Some ice shelves exhibit surface melt ponds before undergoing disintegration, whereas  
others have similar melt ponds but remain intact<sup>6</sup>. Crevassing icequakes could provide  
insight into whether hydrofracture is occurring unnoticed at these apparently stable ice  
shelves, potentially leading to sudden future catastrophic collapse, or whether  
hydrofracture is physically suppressed by another mechanism that affects either the  
stress regime or the fracture toughness of the ice.

In conclusion, understanding the stability of ice sheets and ice shelves is important for sea-level-rise projections<sup>37</sup>. Hydrofracture induced crevassing is an important mechanism that, at least to some extent, controls the stability of such ice bodies. The methodology and findings we present provide a means of attributing crevassing icequakes to hydrofracture. We show that such icequakes can then be used as an observational basis for studying the physical mechanisms associated with hydrofracture induced crevassing.

## Acknowledgements

T. Hudson was funded by a Natural Environment Research Council (NERC) Studentship (NE/L002507/1) for the majority of this work. We thank Antony Butcher for useful conversations regarding the waveform propagation modelling. Seismometers were borrowed from SeisUK and NERC British Antarctic Survey. Seismic data is available from IRIS. Software used includes: QuakeMigrate (<https://github.com/QuakeMigrate>); NonLinLoc (<http://alomax.free.fr/nlloc/>); SeisSrcInv (<https://github.com/TomSHudson/SeisSrcInv>) for the moment tensor inversion; SeisSrcMoment (<https://github.com/TomSHudson/SeisSrcMoment>) for the moment magnitude calculation.

## References

1. Weertman, J. Can a water-filled crevasse reach the bottom surface of a glacier. *IASH publ 95* 139–145 (1973).

- 250 2. Van Der Veen, C. J. Fracture mechanics approach to penetration of surface  
251 crevasses on glaciers. *Cold Reg. Sci. Technol.* **27**, 31–47 (1998).
- 252 3. Das, S. B. *et al.* Fracture propagation to the base of the Greenland Ice Sheet during  
253 supraglacial lake drainage. *Science (80-. )*. **320**, 778–782 (2008).
- 254 4. Rignot, E. & Kanagaratnam, P. Changes in the Velocity Structure of the Greenland  
255 Ice Sheet. *Science (80-. )*. **311**, 986–991 (2006).
- 256 5. Hughes, B. T. On the disintegration of ice shelves: The role of fracture. *J. Glaciol.*  
257 **29**, 98–117 (1983).
- 258 6. Scambos, T. A., Hulbe, C., Fahnestock, M. & Bohlander, J. The link between climate  
259 warming and break-up of ice shelves in the Antarctic Peninsula. *J. Glaciol.* **46**,  
260 (2000).
- 261 7. Scambos, T., Hulbe, C. & Fahnestock, M. Climate-induced ice shelf disintegration in  
262 the Antarctic Peninsula. *Antarct. Penins. Clim. Var. Antarct. Res. Ser.* **79**, 79–92  
263 (2003).
- 264 8. Mcgrath, D. *et al.* Basal crevasses and associated surface crevassing on the Larsen  
265 C ice shelf , Antarctica , and their role in ice-shelf instability. *Ann. Glaciol.* **53**, 10–  
266 18 (2012).
- 267 9. Helmstetter, A., Nicolas, B., Comon, P. & Gay, M. Basal icequakes recorded beneath  
268 an alpine glacier (Glacier d’Argentière, Mont Blanc, France): Evidence for stick-  
269 slip motion? *J. Geophys. Res. Earth Surf.* **120**, 379–401 (2015).
- 270 10. Carmichael, J. D., Pettit, E. C., Hoffman, M., Fountain, A. & Hallet, B. Seismic  
271 multiplet response triggered by melt at Blood Falls, Taylor Glacier, Antarctica. *J.*  
272 *Geophys. Res. Earth Surf.* **117**, 1–16 (2012).
- 273 11. Carmichael, J. D. *et al.* Seismicity on the western Greenland Ice Sheet: Surface  
274 fracture in the vicinity of active moulins. *J. Geophys. Res. Earth Surf.* **120**, 1082–

275 1106 (2015).

276 12. Mikesell, T. D. *et al.* Monitoring glacier surface seismicity in time and space using  
 277 Rayleigh waves. *J. Geophys. Res. Earth Surf.* **117**, 1–12 (2012).

278 13. Neave, K. G. & Savage, J. C. Icequakes on the Athabasca Glacier. *J. Geophys. Res.* **75**,  
 279 1351–1362 (1970).

280 14. Roux, P. F., Walter, F., Riesen, P., Sugiyama, S. & Funk, M. Observation of surface  
 281 seismic activity changes of an Alpine glacier during a glacier dammed lake  
 282 outburst. *J. Geophys. Res.* **115**, 1–13 (2010).

283 15. Walter, F. *et al.* Moment tensor inversions of icequakes on Gornergletscher ,  
 284 Switzerland. *Bull. Seismol. Soc. Am.* **99**, 852–870 (2009).

285 16. Nick, F. M., Van Der Veen, C. J., Vieli, A. & Benn, D. I. A physically based calving  
 286 model applied to marine outlet glaciers and implications for the glacier dynamics.  
 287 *J. Glaciol.* **56**, 781–794 (2010).

288 17. Heyburn, R., Selby, N. D. & Fox, B. Estimating earthquake source depths by  
 289 combining surface wave amplitude spectra and teleseismic depth phase  
 290 observations. *Geophys. J. Int.* **194**, 1000–1010 (2013).

291 18. Jia, Z., Ni, S., Chu, R. & Zhan, Z. Joint inversion for earthquake depths using local  
 292 waveforms and amplitude spectra of Rayleigh waves. *Pure Appl. Geophys.* **174**,  
 293 261–277 (2017).

294 19. Tsai, Y. & Aki, K. Precise focal depth determination from amplitude spectra of  
 295 surface waves. *J. Geophys. Res.* **75**, 5729–5743 (1970).

296 20. Stein, S. & Wiens, D. A. Depth determination for shallow teleseismic earthquakes:  
 297 Methods and results. *Rev. Geophys.* **24**, 806–832 (1986).

298 21. Larsen, S., Wiley, R., Roberts, P. & House, L. *Next-generation numerical modeling:*  
 299 *incorporating elasticity, anisotropy and attenuation. Los Alamos National*



300        *Laboratory* vol. LA-UR-01-1 (2001).

301    22.    Hudson, T. S., Smith, J., Brisbourne, A. & White, R. Automated detection of basal  
302        icequakes and discrimination from surface crevassing. *Ann. Glaciol.* **60**, 1–11  
303        (2019).

304    23.    Buehler, M. J. & Gao, H. Dynamical fracture instabilities due to local  
305        hyperelasticity at crack tips. *Nature* **439**, 307–310 (2006).

306    24.    Tape, W. & Tape, C. A geometric comparison of source-type plots for moment  
307        tensors. *Geophys. J. Int.* **190**, 499–510 (2012).

308    25.    Harper, J. T., Humphrey, N. F. & Pfeffer, W. T. Crevasse patterns and the strain-rate  
309        tensor : a high-resolution comparison. *J. Glaciol.* **44**, (1998).

310    26.    Garcia, L., Luttrell, K., Kilb, D. & Walter, F. Joint geodetic and seismic analysis of  
311        surface crevassing near a seasonal glacier-dammed lake at Gornergletscher,  
312        Switzerland. *Ann. Glaciol.* 1–13 (2019) doi:10.1017/aog.2018.32.

313    27.    Stork, A. L., Verdon, J. P. & Kendall, J. M. The robustness of seismic moment and  
314        magnitudes estimated using spectral analysis. *Geophys. Prospect.* **62**, 862–878  
315        (2014).

316    28.    Podolskiy, E. A. & Walter, F. Cryoseismology. *Rev. Geophys.* **54**, 1–51 (2016).

317    29.    Paterson, W. S. B. *The Physics of Glaciers*. (Butterworth-Heinemann, 1994).

318    30.    Boon, S. & Sharp, M. The role of hydrologically-driven ice fracture in drainage  
319        system evolution on an Arctic glacier. *Geophys. Res. Lett.* **30**, 3–6 (2003).

320    31.    Colgan, W. *et al.* Glacier crevasses: Observations, models, and mass balance  
321        implications. *Rev. Geophys.* **54**, 119–161 (2016).

322    32.    Lipovsky, B. P. & Dunham, E. M. Vibrational modes of hydraulic fractures:  
323        Inference of fracture geometry from resonant frequencies and attenuation. *J.*  
324        *Geophys. Res. Solid Earth* **120**, 1080–1107 (2015).

- 325 33. Jones, G. A., Kulesa, B., Doyle, S. H., Dow, C. F. & Hubbard, A. An automated  
326 approach to the location of icequakes using seismic waveform amplitudes. *Ann.*  
327 *Glaciol.* **54**, 1–9 (2013).
- 328 34. O’Neel, S., Echelmeyer, K. A. & Motyka, R. J. Short-term variations in calving of a  
329 tidewater glacier: LeConte Glacier, Alaska, U.S.A. *J. Glaciol.* **49**, 587–598 (2003).
- 330 35. Krug, J., Weiss, J., Gagliardini, O. & Durand, G. Combining damage and fracture  
331 mechanics to model calving. *Cryosph.* **8**, 2101–2117 (2014).
- 332 36. Pollard, D., DeConto, R. M. & Alley, R. B. Potential Antarctic Ice Sheet retreat  
333 driven by hydrofracturing and ice cliff failure. *Earth Planet. Sci. Lett.* **412**, 112–  
334 121 (2015).
- 335 37. Vaughan, D. . *et al. Chapter 4: Observations: Cryosphere. Climate Change 2013 the*  
336 *Physical Science Basis: Working Group I Contribution to the Fifth Assessment Report*  
337 *of the Intergovernmental Panel on Climate Change* (Cambridge University Press,  
338 Cambridge, United Kingdom and New York, NY, USA, 2013).  
339 doi:10.1017/CBO9781107415324.012.
- 340 38. Gudmundsson, M. T. The Grimsvotn Caldera, Vatnajokull: Subglacial Topography  
341 and Structure of Caldera Infill. *Jokull* **39**, 3–7 (1989).
- 342 39. Björnsson, H. *The Glaciers of Iceland*. (Atlantis Press, 2017). doi:10.2991/978-94-  
343 6239-207-6.
- 344 40. Smith, J. D., White, R. S., Avouac, J.-P. & Bourne, S. Probabilistic earthquake  
345 locations of induced seismicity in the Groningen region, the Netherlands. *Geophys.*  
346 *J. Int.* **222**, 507–516 (2020).
- 347 41. Lomax, A. & Virieux, J. Probabilistic earthquake location in 3D and layered  
348 models. *Adv. Seism. Event Locat. Vol. 18 Ser. Mod. Approaches Geophys.* 101–134  
349 (2000).

42. Hudson, T. S., Brisbourne, A. M., Walter, F., Graff, D. & White, R. S. Icequake source mechanisms for studying glacial sliding. *J. Geophys. Res. Earth Surf. (in Rev.*
43. Prieto, G. A., Parker, R. L. & Vernon, F. L. A Fortran 90 library for multitaper spectrum analysis. *Comput. Geosci.* **35**, 1701–1710 (2009).
44. Krischer, L. mtspec Python wrappers 0.3.2. *Zenodo* doi:10.5281/zenodo.321789.
45. Hanks, T. C. & Kanamori, H. A moment magnitude scale. *J. Geophys. Res.* **84**, 2348 (1979).
46. Mottram, R. H. & Benn, D. I. Testing crevasse-depth models: a field study at Breiðamerkurjökull, Iceland. *J. Glaciol.* **55**, 746–752 (2009).
47. Glen, J. W. The creep of polycrystalline ice. *Proc. R. Soc. Lond. A. Math. Phys. Sci.* **228**, 519–538 (1955).

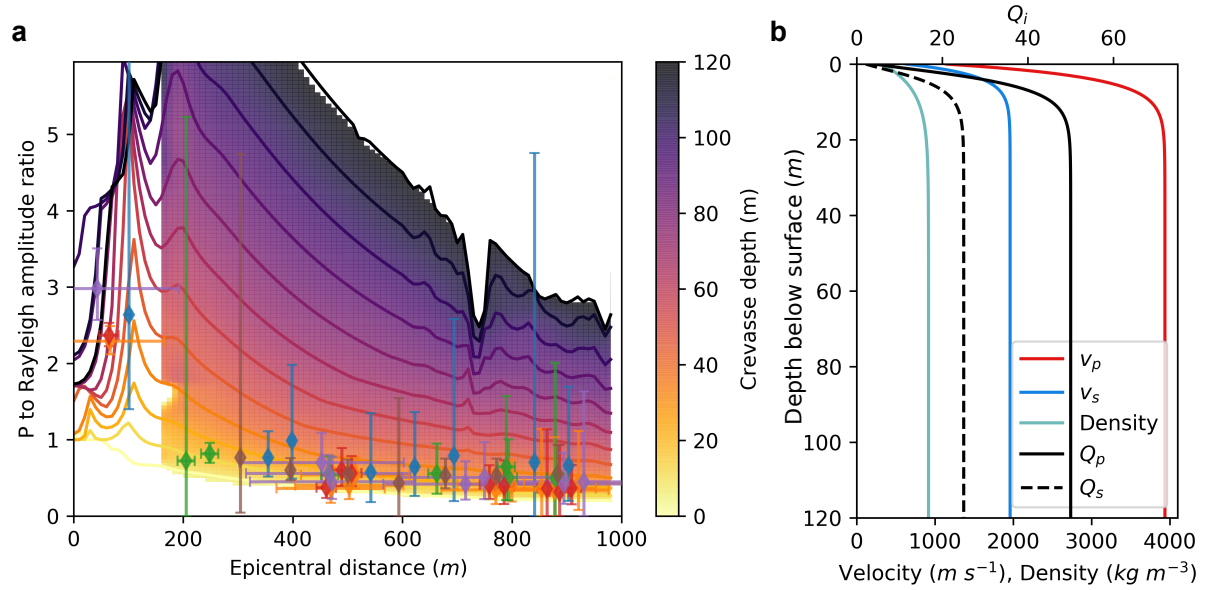
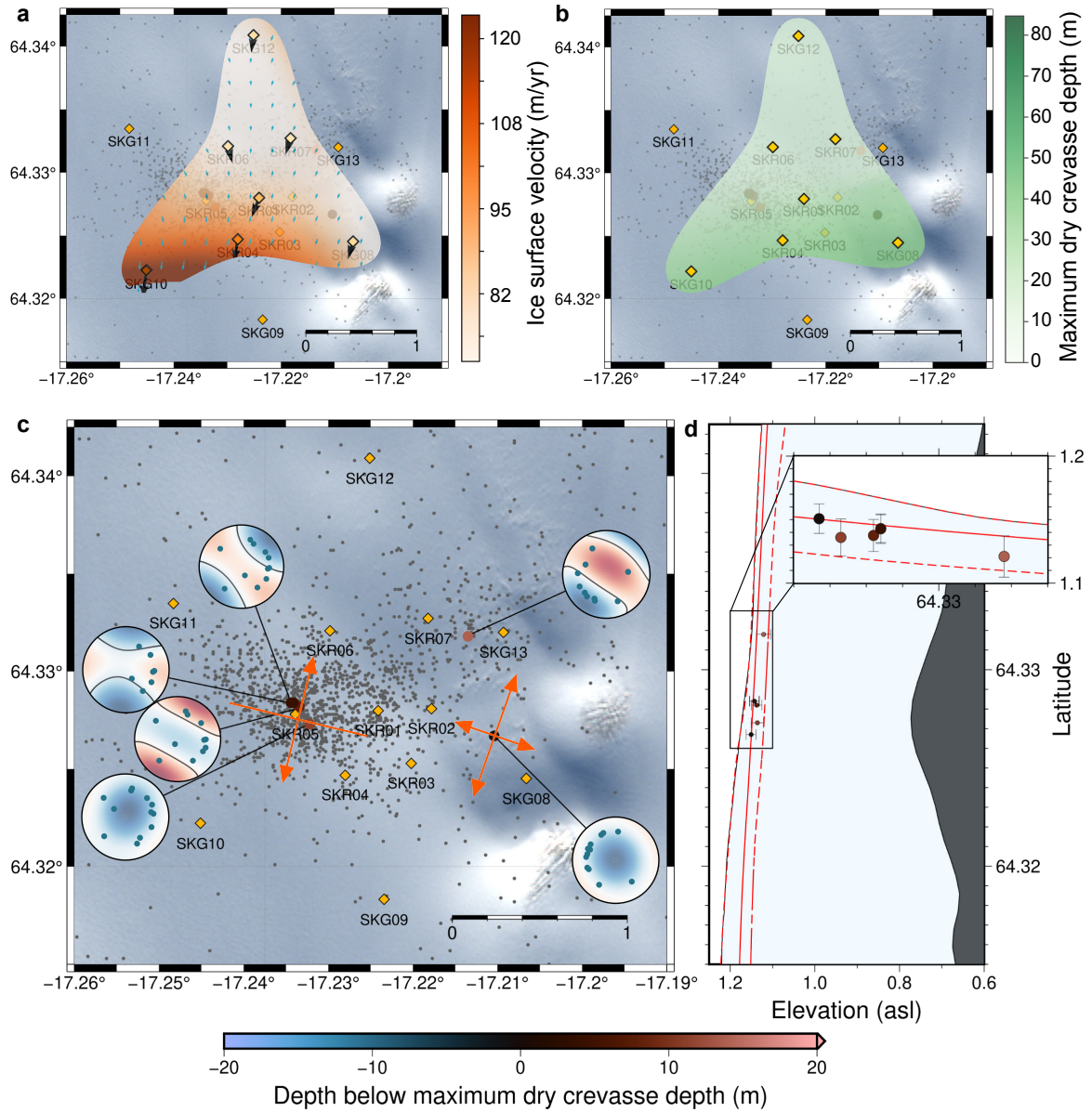


Figure 1 – Obtaining depth for crevassing icequakes. a) Plot of P wave to Rayleigh wave amplitude ratio with epicentral distance from the source. Observed P to Rayleigh amplitudes for the icequakes presented in Figure 2 are plotted (various coloured scatter points). P to Rayleigh amplitudes for modelled crevassing icequakes with source depths from 10 to 120 m below surface are indicated by the solid lines, with the 2D interpolated field plotted at epicentral distances greater than 180 m. b) The velocity model used for the modelled crevassing icequakes<sup>38</sup>.



379

380 *Figure 2 – Summary of crevasse icequake observations. a) The horizontal surface velocity*

381 *field at the site, derived using GPS data from the highlighted stations. b) The maximum-*

382 *dry-crevasse-depth,  $d^*$ , calculated using the velocity field in (a). c) Map of crevasse*

383 *icequake locations. Grey scatter points are all the crevasse icequakes detected during the*

384 *period 19<sup>th</sup> to 29<sup>th</sup> June 2014. The icequakes studied in more detail, with derived depths*

385 *using the P to Rayleigh amplitude method are plotted as larger scatter points, coloured by*

386 *depth below the maximum dry crevasse depth. Upper hemisphere moment tensors for*

387 *these icequakes are also shown. Principal stress vectors derived from the velocity field in*

388 *(a) are shown in orange. Seismometer and geophone locations are shown by the yellow*  
389 *diamonds. Satellite image is from the European Space Agency. d) Plot of the crevassing*  
390 *events in (c) with depth vs. latitude projected onto a N-S transect at 17.225° W. The solid*  
391 *and dashed red lines indicate the maximum dry crevasse depth and the associated*  
392 *uncertainty, respectively. The bed topography is derived from ground-penetrating radar<sup>39</sup>.*

393

394

395

396

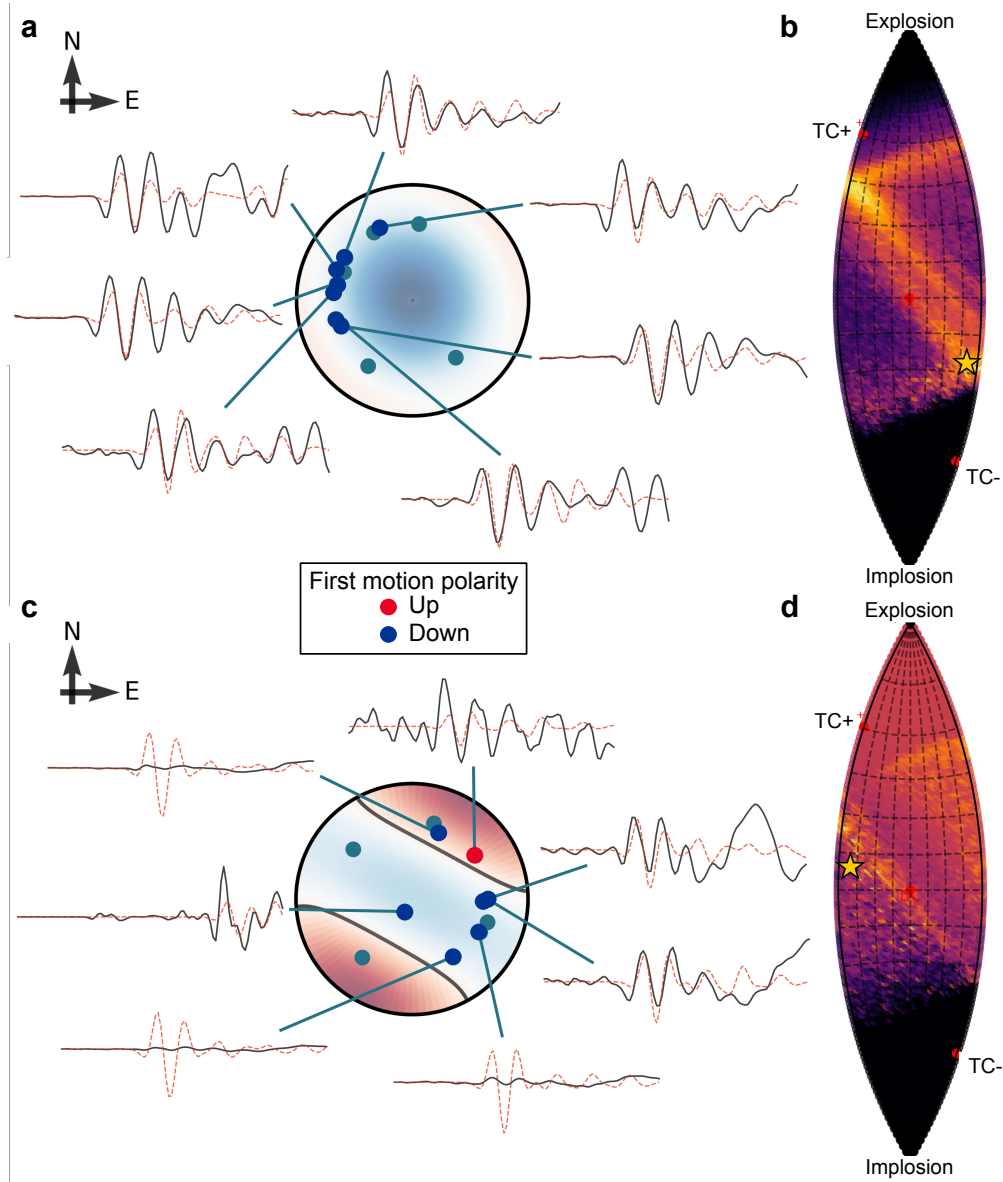


Figure 3 – Examples of upper hemisphere crevasse icequake source mechanisms for two of the events in Figure 2. The source mechanisms are constrained only by P wave phases. a) Source mechanism for a closing-crack crevasse icequake. Black waveforms are observed data, red dashed waveforms are the most likely inversion model result. b) Lune plot (Tape and Tape (2012)) associated with the event in (a), showing the PDF of the full waveform inversion result, indicating the most likely source type. Brighter colours indicate higher probability. c) and d) Same as (a) and (b) except for an opening-crack crevasse icequake.

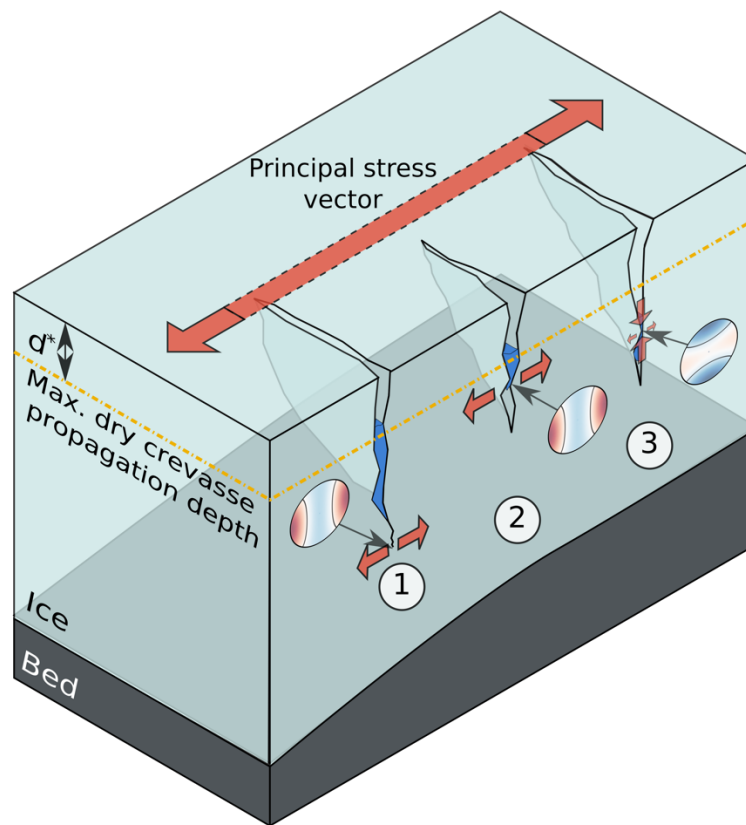


Figure 4 – Interpretation of the possible crevasse failure mechanisms observed. (1) A new opening-crack hydrofracture through previously undamaged ice. (2) An opening-crack hydrofracture of a pre-existing crack. (3) Closing of a pre-existing crack due to the evacuation of water from the crack. Hypothetical source mechanisms are shown for each case.



## Supplementary Information

### Methods

#### Seismicity

The seismicity presented in this study is detected using QuakeMigrate<sup>22,40</sup>, with the method and overall catalogue of icequakes detailed by Hudson et al<sup>22</sup>. We relocate the detected earthquakes using NonLinLoc<sup>41</sup> to obtain more accurate epicentral locations. For the subset of events presented in detail in Figure 1 and 2, we manually pick P and S phase arrivals before relocation. The crevassing icequake hypocentral depths for the selected events are obtained using P to Rayleigh wave amplitude ratios, as described in the main text.

The P to Rayleigh wave amplitude ratios are calculated by taking the maximum amplitude within specified windows, as shown for the observed icequake example in Figure S1a. Figure S1c and Figure S1d show the P and Rayleigh wave phase arrivals for one station ~450 m from the source. The particle motion of the inferred Rayleigh wave is elliptical, providing us with confidence that it is indeed a surface wave arrival. P wave and Rayleigh wave windows are of fixed duration for all events, as in Figure S1. The uncertainty in the observed P to Rayleigh wave amplitude ratios is defined as the standard deviation of the noise signal observed in a window 1s prior to the P phase arrivals. Uncertainty in the epicentral distances given in Figure 1 are defined as the epicentral uncertainty output from NonLinLoc<sup>41</sup>. The same method of obtaining P to Rayleigh wave amplitudes is employed for the 2D finite difference modelled

seismograms for various source depths from E3D<sup>21</sup>. The model is run for various source depths from 10 m to 120 m below surface, with the 2D interpolated field from the model runs (see Figure 1a) used to derive the likely crevasse depth from each receiver observation. These individual receiver observations are then combined for each icequake, to provide an overall estimate of the icequake depth. We independently verify crevasse depth by using S-P delay-times from receivers approximately directly above the crevasse. For the event in Figure S1, the S-P delay-time observed at a receiver approximately above the event is 0.014 s. With the velocity model shown in Figure 1b, this corresponds to an icequake depth of ~25 m below surface, compared to a depth of  $29 \pm 12$  m found using the P to Rayleigh amplitude ratios. We are therefore confident that the P to Rayleigh wave amplitude ratios provide a good estimation of icequake depth.

The icequake source mechanisms are obtained by performing a Bayesian full waveform source inversion using an identical approach to a method detailed by Hudson et al<sup>42</sup>. Only P wave phases are used since the horizontal components are generally too noisy to use, due to the instruments melting out of the glacier. Theoretically, S and surface waves could also be used to constrain the inversion, but the amplitudes of any S arrivals are generally close to the noise levels and we have low confidence in our ability to model the polarity of dispersive surface waves sufficiently accurately for a moment tensor inversion, given the depth dependent velocity structure of the firn layer at the site. We use a finite difference scheme to model the Green's functions used to produce the synthetic seismograms in the inversion. The depth of the source, a critical parameter affecting the source inversion, is constrained using P to Rayleigh amplitude ratios.

The moment magnitude,  $M_w$ , of the icequakes is calculated using a spectral method<sup>27</sup>.

The spectrum of the icequake is calculated by performing multi-taper spectral estimation<sup>43,44</sup> in order to find the long period spectral level and hence the seismic moment release,  $M_0$ .  $M_w$  can then be calculated from<sup>45</sup>,

$$M_w = \frac{2}{3} \log_{10}(M_0) - 6.0. \quad (1)$$

If one assumes that all the moment release for a given icequake is released via tensile failure, then the opening of a crack,  $\Delta V$ , can be calculated from,

$$\Delta V = \frac{M_0}{\sigma_T} \quad (2)$$

where  $\sigma_T$  is the tensile strength of the ice, taken to be 1.5 MPa<sup>28</sup> in this study.

#### Derivation of maximum-dry-crevasse-depth

The maximum depth to which a crevasse can propagate without hydrofracture is governed by the tensile stress regime near the glacier surface. If the ice is under tensile stress then a crevasse can form. However, as the depth through the ice increases, the ice overburden pressure increases and acts to close the crevasse and prevent further fracture. At a certain depth, the maximum-dry-crevasse-depth,  $d^*$ , the maximum principal tensile stress acting to open crevasses becomes equal to the compressive ice overburden pressure. Below this depth, the ice overburden pressure is sufficiently high to prevent opening. This crevassing model is commonly referred to as the zero stress model<sup>31</sup>, and has been proven effective in predicting real crevasse depths<sup>46</sup>.

The above statement assumes that the ice will open under any net tensile stress, which is not strictly correct since the ice also has a tensile failure strength, that we do not account for here. Accounting for the tensile strength of the ice would simply make  $d^*$  shallower and hence increase the depth difference between icequake depths and the maximum-dry-crevasse-depth equipotential, therefore increasing the likelihood of icequakes observed being associated with hydrofracture. We also assume that there is a shallow firn layer at the glacier surface, of lower density than the underlying ice. This lower-density layer acts to make the maximum-dry-crevasse-depth deeper. We use the same local seismic refraction survey<sup>38</sup> as used to constrain the seismic velocities in Figure 1 to constrain the density profile of this layer, making the assumption that the change in velocity in the firn-layer is dominated by density rather than the bulk and shear moduli. This simplified firn density correction is assumed adequate for the purposes of this study since the weight estimation of the firn layer is conservative, therefore resulting in an overestimate of the maximum-dry-crevasse-depth.

To find  $d^*$ , one has to calculate the stress field near the glacier surface. This can be approximately obtained using the glacier surface velocity field. For a given point on the glacier, the velocity is defined by,

$$\overrightarrow{v_{i,j}} = \begin{pmatrix} u_{i,j} \\ v_{i,j} \\ w_{i,j} \end{pmatrix}, \quad (3)$$

where  $u$ ,  $v$  and  $w$  are the velocities in the  $x$ ,  $y$  and  $z$  directions, and  $i, j$  denotes a particular horizontal location within the velocity field. To obtain the velocity field for the glacier surface at Skeidararjökull, we use GPS location data from the seismometers shown in Figure 2. The GPS data from the seismometers is more poorly constrained compared to dedicated dual-frequency GPS instruments, and is sampled only once per

hour. Therefore, in order to reduce the GPS noise, we use a seven day moving average for the latitude, longitude and elevation data. We then calculate the average velocity over the ten day period of analysis. Even after applying this processing, data from only 7 stations are of sufficient quality to use. We then perform a two-dimensional, second-order interpolation for these velocity data points in order to obtain a horizontal velocity field for the network area. Due to only one station, SKR12, constraining the velocity field for the upper half of the network area, the interpolation scheme performs poorly outside the network, so we only analyse the velocity field approximately within the network, as shown in Figure 2 and Figure S2.

The velocity field can then be used to obtain the strain rate field for each point (x,y,z) on the glacier surface. The second order strain rate tensor is given by,

$$\dot{\epsilon}_{i,j} = \begin{pmatrix} \dot{\epsilon}_{xx} & \dot{\epsilon}_{xy} & \dot{\epsilon}_{xz} \\ \dot{\epsilon}_{xy} & \dot{\epsilon}_{yy} & \dot{\epsilon}_{yz} \\ \dot{\epsilon}_{xz} & \dot{\epsilon}_{yz} & \dot{\epsilon}_{zz} \end{pmatrix} = \begin{pmatrix} \frac{\partial u_{i,j}}{\partial x} & \frac{1}{2} \left( \frac{\partial u_{i,j}}{\partial y} + \frac{\partial v_{i,j}}{\partial x} \right) & 0 \\ \frac{1}{2} \left( \frac{\partial u_{i,j}}{\partial y} + \frac{\partial v_{i,j}}{\partial x} \right) & \frac{\partial v_{i,j}}{\partial y} & 0 \\ 0 & 0 & \frac{\partial w_{i,j}}{\partial z} \end{pmatrix}. \quad (4)$$

$\dot{\epsilon}_{xz}$  and  $\dot{\epsilon}_{yz}$  are taken to be zero, assuming no shear with depth, a realistic approximation near the glacier surface. If one also assumes that ice is incompressible, then  $tr(\dot{\epsilon}) = 0$ .

$\dot{\epsilon}_{zz}$  can then be found, giving,

$$\dot{\epsilon}_{zz} = \frac{\partial w_{i,j}}{\partial z} = - \left( \frac{\partial u_{i,j}}{\partial x} + \frac{\partial v_{i,j}}{\partial y} \right). \quad (5)$$

To find the maximum-dry-crevasse-depth, we require the stress tensor. In order to calculate the stress tensor from the strain tensor, we need one final piece of information, the effective viscosity,  $\eta_{eff}$ , for a given horizontal location. Since ice

behaves as a non-linear fluid,  $\eta_{eff}$  varies with the strain rate,  $\dot{\epsilon}$ . The effective viscosity is defined as,

$$\eta_{eff,i,j} = \frac{B}{2} (\dot{\epsilon}_{eff,i,j})^{\frac{1}{n}-1}, \quad (6)$$

where B is given by,

$$B = A^{-\frac{1}{n}}, \quad (7)$$

where the temperature-dependent rate factor  $A = 5.6 \times 10^{-17} Pa^{-3} a^{-1}$  and  $n = 3$ , determined from laboratory studies<sup>16,47</sup>. The effective strain rate,  $\dot{\epsilon}_{eff}$ , is defined by,

$$\dot{\epsilon}_{eff,i,j} = |\dot{\epsilon}_{i,j}| = \left( \frac{1}{2} tr(\dot{\epsilon}_{i,j} \cdot \dot{\epsilon}_{i,j}) \right)^{\frac{1}{2}}. \quad (8)$$

At the maximum-dry-crevasse-depth, the deviatoric stress tensor can then be set equal to the ice overburden pressure stress tensor,

$$\sigma_{overburden} = \sigma_{deviatoric}, \quad (9)$$

which can be written explicitly as,

$$\rho g(d_{i,j}^* - z) \mathbf{I} = \begin{pmatrix} 4\eta_{eff,i,j}\epsilon_{xx,i,j} + 2\eta_{eff,i,j}\epsilon_{yy,i,j} & 2\eta_{eff,i,j}\epsilon_{xy,i,j} & 0 \\ 2\eta_{eff,i,j}\epsilon_{xy,i,j} & 4\eta_{eff,i,j}\epsilon_{yy,i,j} + 2\eta_{eff,i,j}\epsilon_{xx,i,j} & 0 \\ 0 & 0 & 0 \end{pmatrix}, \quad (10)$$

where  $\sigma_{deviatoric,xz}$  and  $\sigma_{deviatoric,yz}$  are zero since we have assumed no vertical shear stress with depth and  $\sigma_{deviatoric,zz}$  is zero assuming that the ice is incompressible.

Finally, to find  $d^*$  we need to find the maximum principal deviatoric stress,  $\sigma_{deviatoric}^*$ .

To do this, we rotate  $\sigma_{deviatoric}$  to maximise the tensile deviatoric stress,

$$\sigma_{deviatoric,i,j}^* = \mathbf{S} \sigma_{deviatoric,i,j} \mathbf{S}^T, \quad (11)$$

where  $\mathbf{S}$  is a rotation matrix comprising the eigenvectors of  $\sigma_{deviatoric}$ . The maximum-

dry-crevasse-depth at a given point on the glacier surface,  $d_{i,j}^*$ , is then given by<sup>16</sup>,

$$d_{i,j}^* = \frac{\max(\sigma_{deviatoric,i,j}^*)}{\rho g}. \quad (12)$$

The uncertainty associated with the maximum-dry-crevasse-depth field is proportional to the uncertainty in the velocity field. To estimate the uncertainty, we calculate the standard deviation in the average velocity data and randomly perturb the velocity data used to calculate the velocity field by gaussian distributions about the average observed velocities, with the standard deviations used to constrain the width of these distributions. These gaussian distributions are sampled 1000 times. We then calculate the strain, stress, and crevasse depth fields from each perturbed velocity field, and define the lower and upper uncertainties for each field as the minimum and maximum values, respectively, for each point spatially within the fields. This data is shown by the red dashed lines in Figure 2d, and all the fields and their associated uncertainties are shown in Figure S2.

584  
585  
586  
587  
588  
589  
590  
591  
592  
593  
594  
595  
596  
597  
598  
599  
600  
601  
602  
603  
604  
605



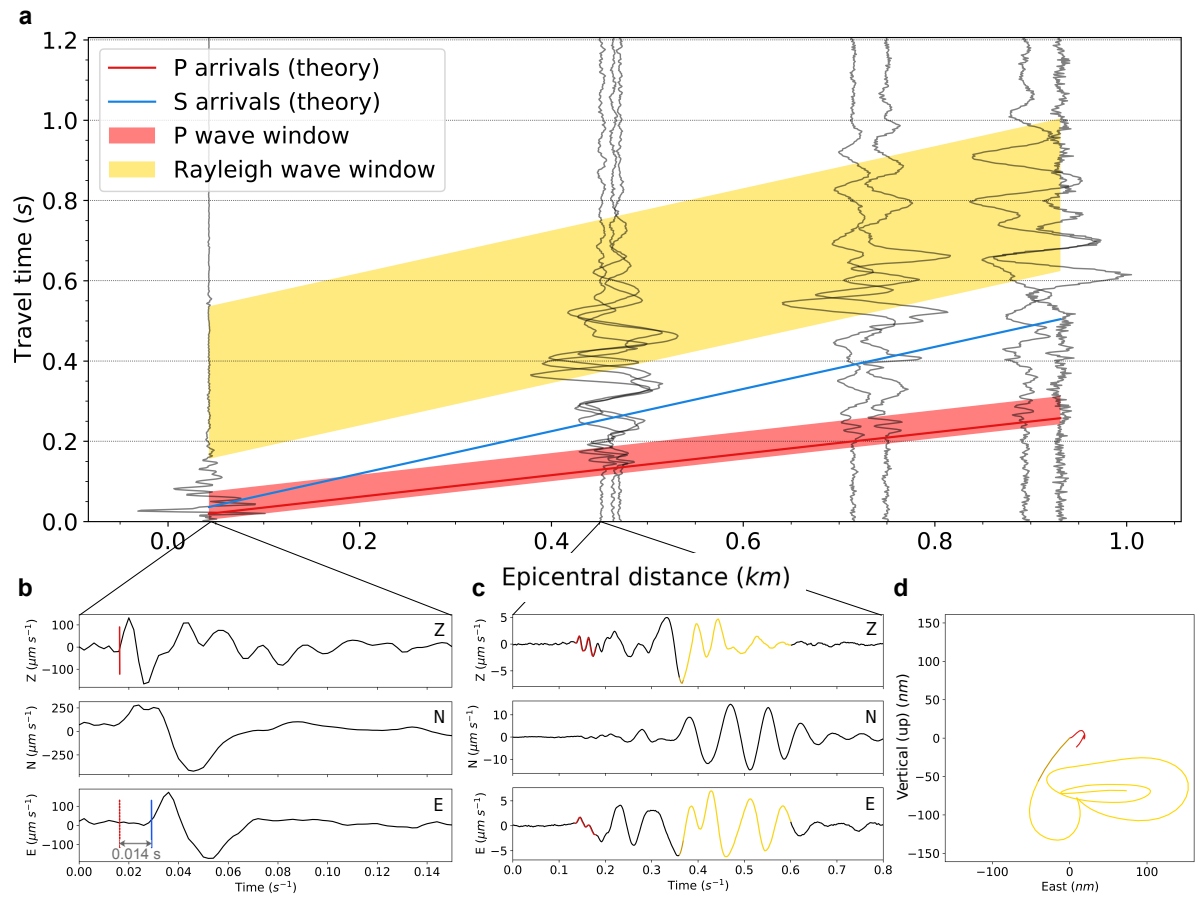


**Figure S1 – Example of observed waveforms at seismometers from a crevasse icequake at 14:33:52 on 28<sup>th</sup> June 2014. a) Record section showing the P and Rayleigh wave arrivals. The red and yellow regions show the windows used to calculate the P to Rayleigh amplitude ratios. b) Waveforms for an arrival 43 m from the event epicentre. P and S phase arrivals are indicated by the red and blue lines, respectively. c) Waveforms for an arrival 450 m from the event epicentre. d) Particle motions associated with the P and Rayleigh phase arrivals in (c). Red is the P wave phase and yellow is the Rayleigh wave phase.**

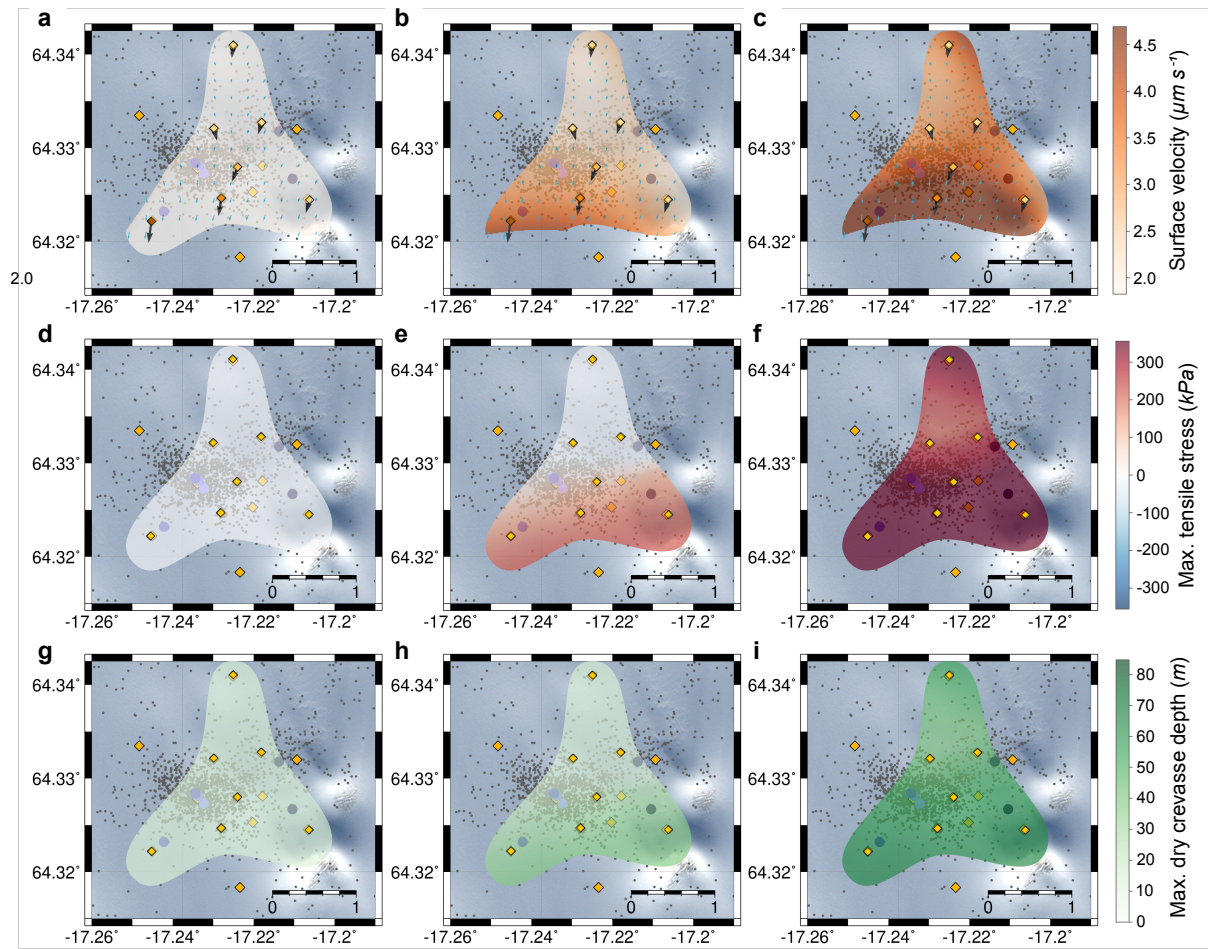


Figure S2 - The estimated uncertainty in the interpolated maximum surface velocity, maximum principal tensile stress and maximum-dry-crevasse-depth fields. (a) to (c) The lower, actual and upper uncertainty associated with the surface velocity field, respectively. (d) to (f) The lower, actual and upper uncertainty associated with the maximum principal stress field, respectively. (g) to (i) The lower, actual and upper uncertainty associated with the maximum-dry-crevasse-depth, respectively.